J. Phys. Chem. A **2001,** *105,* 6655−6667

Kinetics and Mechanism of the Reactions of Ground-State Y ($4d^15s^2$, ^2D) with Ethylene and Propylene: Experiment and Theory

Meredith Porembski and James C. Weisshaar*

Department of Chemistry, University of Wisconsin−*Madison, 1101 University Avenue,*
Madison, Wisconsin 53706-1396

Received: February 18, 2001; In Final Form: May 3, 2001

Bimolecular rate constants, primary products, and kinetic isotope effects for the reactions of Y ($4d^15s^2$, ^2D) with C_2H_4 and C_2D_4 and with C_3H_6 and C_3D_6 are measured in a fast flow reactor at 300 K with He/N_2 buffer gas at 0.8 Torr. The H_2 and D_2 elimination products and Y(alkene)-stabilized complexes are detected using single photon ionization at 157 nm and time-of-flight mass spectrometry. We find a small normal isotope effect ($k_H/k_D = 1.75 \pm 0.12$) for the reaction with ethylene but no significant isotope effect ($k_H/k_D = 1.06 \pm 0.07$) for the reaction with propylene. We use density functional theory in its B3LYP and *m*PW1PW91 forms with a large basis set to characterize stationary points on the doublet potential energy surface for the reaction $Y + C_2H_4 \rightarrow YC_2H_2 + H_2$. Theory finds no energy barrier to the formation of a long-range Y−ethylene complex. Subsequent steps involving CH bond insertion by metallacyclopropane complexes are consistent with earlier work. However, a new, low-energy path involves concerted rearrangement of the HYC_2H_3 insertion intermediate directly to a weakly bound, product-like complex with no exit channel barrier to elimination products. Theory also provides a set of geometries and vibrational frequencies for use in statistical rate models of the hot metallacyclopropane complex decay. The preferred model, consistent with the collection of Y + ethylene experimental data, requires no adjustments to the *m*PW1PW91 energies. As in earlier work, B3LYP places key transition state energies too high by 6−9 kcal/mol. The available evidence suggests that nonadiabatic and/or steric effects contribute to the reaction inefficiency at room temperature.

I. Introduction

In the past decade, considerable experimental and theoretical effort has been devoted to the study of the reactivity of ground-state transition metal atoms Y, Zr, and Nb with alkenes.[1−17] Such work has the potential to improve our understanding of the polymerization of olefins by transition metal compounds via the Ziegler−Natta process.[18−20] We and others have used fast flow reactors equipped with laser-induced fluorescence (LIF) detection of metal atoms to determine room-temperature chemical reaction kinetics.[1−4] Identification of reaction products is now possible using photoionization mass spectrometry (PIMS) at 157 nm.[5,6] The chemical reaction dynamics of Y, Zr, and Nb with ethane, ethylene, or acetylene have been studied in a crossed-beam apparatus equipped with PIMS detection at higher collision energies.[7−9]

The bulk of the theoretical work on the interaction of second-row transition metals with small alkenes must be credited to Siegbahn, Blomberg, and others.[11−17] For the Y + ethylene reaction, the studies identified those stationary points expected to be involved in primary CH bond insertion, including the strongly bound metallacyclopropane complex YC_2H_4, a CH insertion transition state, and an insertion intermediate HYC_2H_3.[11,12,15] On the basis of the calculated exothermicity of the $YC_2H_2 + H_2$ products (−11.5 kcal/mol) and relatively small CH insertion barrier (+1.9 kcal/mol), it was suggested that ground-state Y should effect bimolecular H_2 elimination from ethylene at room temperature;[3] however, detailed mechanistic questions remain. To date, no study has investigated the possible existence of a barrier to the approach of Y with ethylene along the adiabatic entrance channel, explicitly confirmed the mechanism of primary CH insertion or determined the mechanism of H_2 elimination from the insertion intermediate HYC_2H_3.

More recently, we have performed extensive density functional theory (DFT) calculations for the Zr ($4d^25s^2$, ^3F) + ethylene reaction, following the evolution of ground-state reactants to H_2 elimination products on both the triplet and singlet potential energy surfaces (PESs).[10] Statistical rate modeling suggests that the hybrid density functional B3LYP[21] places key transition state energies too high by 6−9 kcal/mol, while the *m*PW1PW91[22,23] functional gives much more realistic energies. This is consistent with the performance of B3LYP in similar studies involving transition metal *cations* and small alkanes.[24−27]

Toward a comprehensive and consistent mechanistic picture of TM + alkene systems, we extend the joint experimental and theoretical approach to the reactions of Y ($4d^15s^2$, ^2D) with ethylene and propylene. For the first time, we report the primary products and kinetic isotope effects at 300 K for the reactions of Y with C_2H_4, C_2D_4, C_3H_6, and C_3D_6. Bimolecular H_2 elimination products are observed for all four reactions, which corroborates a significant theoretical prediction.[3] Stabilized Y(alkene) complexes are also detected for the reactions with C_2D_4, C_3H_6, and C_3D_6. A small positive isotope effect is measured for Y + ethylene, while undeuterated and deuterated propylene react with Y at essentially the same rate.

This paper also presents a detailed theoretical study of Y ($4d^15s^2$, ^2D) + ethylene using the B3LYP and *m*PW1PW91 functionals with a large basis set, including complete charac-

---

* To whom correspondence should be addressed. E-mail: weisshaar@chem.wisc.edu.

10.1021/jp010646t CCC: $20.00

terization of all intermediates and transition state structures along the doublet PES. Theory identifies the entrance channel transition state $^2\mathbf{TS_{ent}}$, although both DFT methods find it to lie essentially isoenergetic to ground-state reactants. We locate the metallacyclopropane complex YC_2H_4 and the CH insertion transition state $^2\mathbf{TS_{ins}}$, calculating rotational constants and vibrational frequencies for use in the statistical rate models. Similar to our recent investigation of the triplet Zr + ethylene PES,[10] we find that the doublet Y + ethylene PES branches from the insertion intermediate HYC_2H_3 into two low-lying paths. The higher energy, stepwise rearrangement path passes through a dihydrido intermediate and over a substantial exit barrier $^2\mathbf{TS_{exit}}$ lying 23 kcal/mol above products. The lower energy path directly connects HYC_2H_3 to a product-like complex $H_2{-}YC_2H_2$ via a multicenter transition state $^2\mathbf{MCTS}$. In this concerted rearrangement mechanism, the product-like complex dissociates to YC_2H_2 ($^2A_1$) + H_2 products with no barrier.

Finally, we use RRKM[28,29] statistical rate modeling based on the electronic structure calculations to determine the adjusted energies of key stationary points involved in primary CH bond insertion that bring the model results in accord with all of the experimental data. Our preferred model successfully predicts the observed Y + ethylene isotope effect and branching ratios, requiring essentially no adjustments to the *m*PW1PW91 energies. As before,[10] the B3LYP value of $^2\mathbf{TS_{ins}}$ is found to be at least 6−9 kcal/mol too high. This suggests that nonadiabatic or steric effects play an important role in controlling the overall reaction efficiency of ground-state Y and Zr with small alkenes.

II. Experimental Section

A. Methods. An earlier publication describes our flow tube apparatus and the PIMS technique in detail.[5] Briefly, we use laser ablation to generate gas-phase transition metal atoms in a fast flow of predominately He and some N_2 (added to quench He* and Y* metastable states). The flow tube temperature is 300 K, and the pressure may vary from 0.5 to 1.1 Torr, with N_2 partial pressure constant at 120 mTorr. Frequent collisions with the buffer gas thermalize metal atoms as they travel down the flow tube. In the reaction zone, hydrocarbon flow is regulated by a flow controller and monitored by a mass flow meter (Tylan). Hydrocarbon gases C_2H_4 (Matheson 99.99%), C_2D_4 (Cambridge Isotopes 98%), C_3H_6 (Matheson 99.6%), and C_3D_6 (Cambridge Isotopes 98%) were used directly from the bottle. Because flow meter response is not linear with gas flow, we calibrate the flow meters with each reactant gas, measuring pressure vs time while flowing gas into a calibrated volume. Calibration curves for deuterated and undeuterated gases are noticeably different. A skimmer (floated at +8 V) terminates the reaction and permits neutral species to proceed to the detection region where a 157 nm, 7.9 eV laser (Lambda Physik, LPX 210i) ionizes unreacted metal and metal products. The ions are collected via time-of-flight mass spectrometry (TOF-MS).

By measuring integrated ion currents as a function of hydrocarbon flow at a fixed mean reaction time, we extract effective bimolecular rate constants. A variety of complications such as ion−molecule reactions, excited-state reactions, multiphoton effects, and photoionization followed by fragmentation of reaction products and have been considered and were found to be minimized under our experimental conditions.[5] The good agreement with rate constants derived from state-specific laser-induced fluorescence (LIF) data[2] confirms that we are probing ground-state reactions with the PIMS technique.

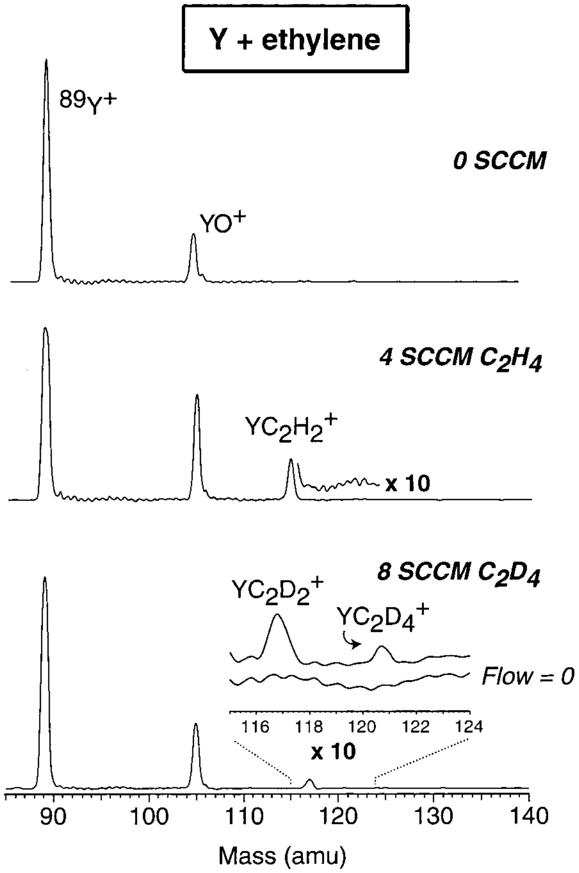

Figure 1. Time-of-flight mass spectra for Y without ethylene flow and with C_2H_4 and C_2D_4 flow as indicated.

B. Results. Figure 1 shows typical photoionization mass spectra taken with zero hydrocarbon flow and with small flows of either C_2H_4 or C_2D_4. At zero hydrocarbon flow we observe Y^+ (89 amu, 100% natural abundance) and YO^+; the latter is likely from YO ablated from the oxidized metal surface. As alkene flow increases, both Y^+ and YO^+ signals decrease while the metal-containing hydrocarbon products labeled in Figure 1 emerge. We find that the primary products of the reactions of Y with C_2H_4 and C_2D_4 are:

$$Y + C_2H_4 \xrightarrow{>90\%} YC_2H_2 + H_2 \tag{1}$$

$$Y + C_2D_4 \xrightarrow{67\%} YC_2D_2 + D_2 \tag{2}$$

$$\xrightarrow{33\%} YC_2D_4$$

Multiphoton effects are negligible as we observe that neither the products present in the mass spectra nor their relative intensities change with laser fluence over at least a factor of 10.

In the absence of experimental complications (see below), the PIMS ion intensities reflect the partitioning of internally hot collision complexes between elimination and collisional stabilization product channels. For the Y + C_2H_4 reaction, we estimate that collisionally stabilized YC_2H_4 complexes are less than 10% of the primary products over a flow tube pressure range of 0.5 to 1.1 Torr. For the Y + C_2D_4 reaction, a fraction of the collision complexes *are* stabilized and subsequently ionized to $YC_2D_4^+$. Branching ratios, defined as the ratio of stabilized complexes to elimination products, are listed in Table 1. Our ability to measure the product peak integrals is limited by experimental signal-to-noise and mass-resolution. The precision of the resulting branching ratios is reported as $\pm 1\sigma$.

TABLE 1: Primary Reaction Products, Branching Ratios, Effective Bimolecular Rate Constants, and Resulting Isotope Effects for the Reaction of Y($4d^15s^2$, ^2D) with Alkenes at 0.8 ± 0.05 Torr He/N_2 and 300 ± 5 K

alkene	primary reaction product	branching ratio[b]	k (10^{-12} cm^3 s^{-1})[c]	k_H/k_D
C_2H_4	>90% YC_2H_2	0.10 ± 0.03	7.4 ± 0.3	
C_2D_4	67% YC_2D_2 33% YC_2D_4	0.33 ± 0.09	4.2 ± 0.12	1.75 ± 0.12
C_3H_6	8% YC_3H_2 48% YC_3H_4 44% YC_3H_6	0.79 ± 0.15	122 ± 7	
C_3D_6	10% YC_3D_2 32% YC_3D_4 58% YC_3D_6	1.38 ± 0.21	116 ± 2	1.06 ± 0.07

[a] Inferred from photoionization mass spectra. [b] The ratio of stabilized Y(alkene) complexes to elimination products, assuming comparable reactivities and photoionization cross-sections of the primary reaction products (see text for details). The uncertainties refer to the precision of experiments; ± 1σ of the mean of five values in the case of Y + ethylene, and 10 values in the case of Y + propylene. [c] Uncertainties refer to the precision of experiments; ± 1σ of the mean of three to five values. Absolute accuracy of rates is ± 30%. Rate constants measured at 0.8 Torr He/N_2 and 300 K with LIF detection are 8.2 ± 0.8 × 10^{-12} cm^3 s^{-1}and 141 ± 14 × 10^{-12} cm^3 s^{-1} for the Y($^2D_{3/2}$) reaction with C_2H_4 and C_3H_6, respectively (ref 2).

Although we do not detect the primary products of the YO + ethylene reactions, possibly the result of a higher ionization potential and/or smaller photoionization cross-section, products from the reaction with a second and third ethylene molecule are observed (not shown).

Similarly, as shown in Figure 2, we find the primary products of the reactions of Y with C_3H_6 and C_3D_6 to be:

$$\begin{aligned} Y + C_3H_6 &\xrightarrow{8\%} YC_3H_2 + 2H_2 \quad (3)\\ &\xrightarrow{48\%} YC_3H_4 + H_2\\ &\xrightarrow{44\%} YC_3H_6 \end{aligned}$$

$$\begin{aligned} Y + C_3D_6 &\xrightarrow{10\%} YC_3D_2 + 2D_2 \quad (4)\\ &\xrightarrow{32\%} YC_3D_4 + D_2\\ &\xrightarrow{58\%} YC_3D_6 \end{aligned}$$

Branching ratios are included in Table 1. Again, we find that neither the products nor their relative intensities change with laser fluence. While double dehydrogenation of alkenes by neutral transition metal atoms has not been previously reported, double H_2 elimination of alkanes and alkenes by the early 3d transition metal *ions* is well documented.[30−38] The primary products of the YO + $C_3H(D)_6$ reactions are detected, also labeled in Figure 2.

The secondary reactions of Y and YO with all four hydrocarbons will not be discussed here. Briefly, Y reacts successively with four molecules of C_2H_4 or C_2D_4 and with three molecules of C_3H_6 or C_3D_6. Alkene addition, rather than elimination of H_2 or D_2, is increasingly favored as the number of ligands surrounding the metal increases.

Representative pseudo-first-order kinetics plots for the Y + ethylene and Y + propylene reactions are shown in Figure 3 and Figure 4, respectively. The resulting effective bimolecular rate constants at 300 K and 0.8 Torr total pressure are also collected in Table 1 for all four reactions. Each rate constant is the mean of at least three experiments and in most cases five.

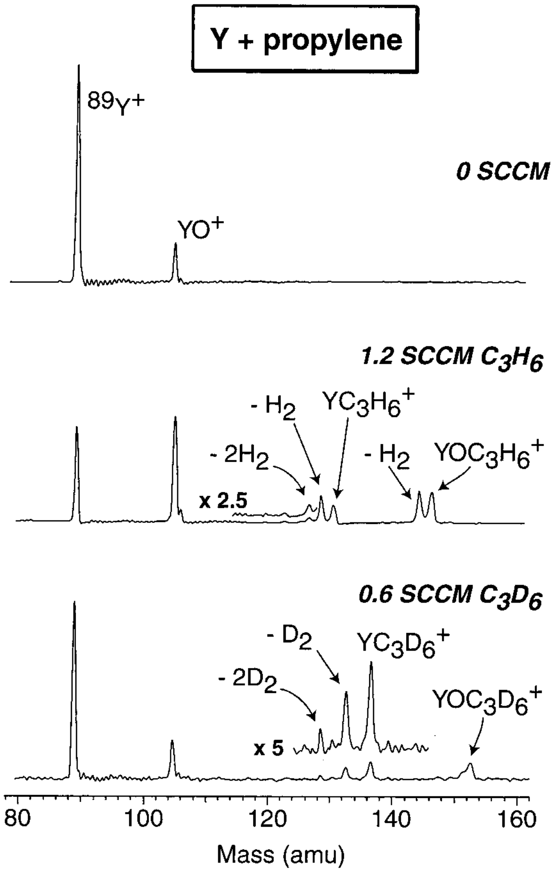

Figure 2. Time-of-flight mass spectra for Y without propylene flow and with C_3H_6 and C_3D_6 flow as indicated.

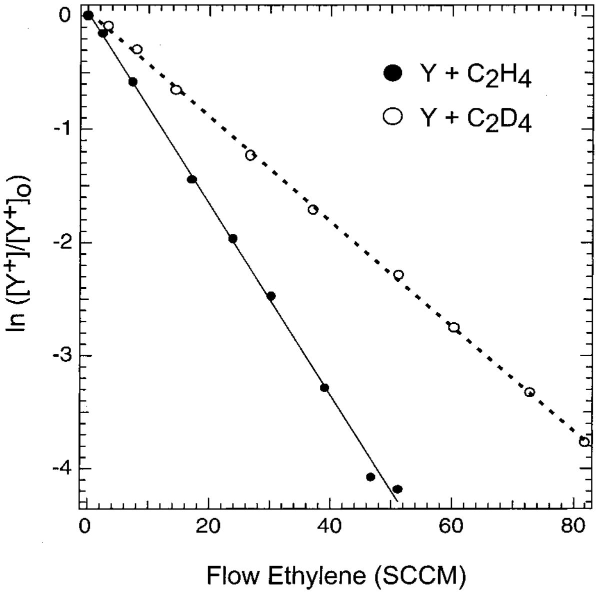

Figure 3. Semilogarithmic plots of metal atom density, proportional to integrated ion current, vs hydrocarbon flow for Y + C_2H_4 and Y + C_2D_4 reactions.

For comparison, we include the rate constants for Y ($4d^15s^2$, $^2D_{3/2}$) + C_2H_4 and Y ($4d^15s^2$, $^2D_{3/2}$) + C_3H_6 as measured with LIF detection[2] (footnote c in Table 1). The absolute accuracy of our measurements is ± 30% due to uncertainties in the mean reaction time, flow calibrations, etc. However, the typical precision of the experiments is much higher. Since most systematic errors should cancel for ratios of rate constants and we have corrected for different flow calibrations, we estimate

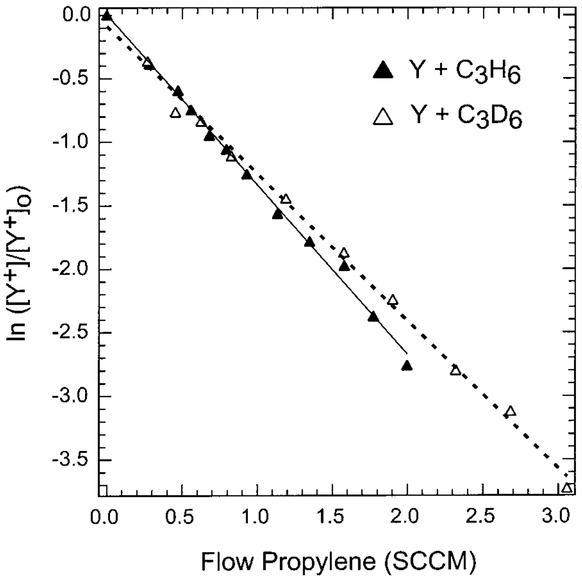

Figure 4. Semilogarithmic plots of metal atom density, proportional to integrated ion current, vs hydrocarbon flow for Y + C_3H_6 and Y + C_3D_6 reactions.

TABLE 2: Calculated Energies (kcal/mol) of Stationary Points along the Y + Ethylene Doublet PES[a]

species	MCPF+ PCI-80[b]	B3LYP/Stuttgart+ 6-311++G(d,p)	*m*PW1PW91/ Stuttgart+ 6-311++G(d,p)[c]
$^{2}\mathbf{TS}_{\mathbf{ent}}$		−0.28 (−0.33)	−1.4 (−1.5)
$Y{-}C_2H_4$ ($^2B_2$) (**1a**)		−16.3 (−16.2)	
YC_2H_4 ($^2A_1$) (**1b**)	−27.7	−22.3 (−22.0)	−31.0 (−30.7)
$^{2}\mathbf{TS}_{\mathbf{ins}}$	+1.9	+4.8 (+5.9)	−3.0 (−1.8)
nonplanar HYC_2H_3 (**2a**)	−27.4	−22.8 (−21.6)	−27.3 (−26.1)
planar HYC_2H_3 (**2b**)		−23.3 (−21.9)	−27.3 (−26.0)
$^{2}\mathbf{TS}_{\beta\mathbf{H}}$		+4.3 (+6.9)	+0.26 (+2.9)
^{2}**MCTS**		−1.0 (+0.66)	−7.9 (−6.3)
$H_2Y{-}C_2H_2$ (**3a**)		−9.0 (−6.3)	−11.7 (−9.0)
$H_2{-}YC_2H_2$ (**3b**)		−2.2 (−0.84)	−7.9 (−6.5)
$^{2}\mathbf{TS}_{\mathbf{exit}}$		+19.9 (+22.7)	+15.0 (+17.9)
$Y{-}C_2H_2$ ($^2B_2$) + H_2 (**4a**)		+19.3 (+21.8)	
YC_2H_2 ($^2A_1$) + H_2 (**4b**)	−11.5	−3.2 (−0.99)	−7.6 (−5.4)
YH_2 ($^2A_1$) + C_2H_2	+19.1[e]	+17.3 (+20.1)	

[a] Energies relative to free reactants, corrected for differential zero-point energy effects. Parentheses denote energetics for Y + C_2D_4. [b] MCPF+PCI-80 calculations by Blomberg and Siegbahn from ref 3, unless otherwise indicated. Geometries of these species were not described. [c] Single-point energies for all structures optimized at the level of B3LYP/Stuttgart 6-311++G(d,p). [e] Estimated exothermicity using the heat of formation of C_2H_2 and the calculated binding energy of YH_2 ($^2A_1$) from Siegbahn, P. E. M. *Theor. Chim. Acta* **1994**, 87, 441.

that the ratios k_H/k_D in Table 1 are accurate to within ± 7% for the reactions with ethylene and propylene. There is a small normal deuterium isotope effect with ethylene ($k_H/k_D = 1.75 \pm 0.12$) and no isotope effect with propylene within experimental uncertainty ($k_H/k_D = 1.06 \pm 0.07$).

For purposes of our statistical rate modeling efforts (Section IV), we assume that the chemical branching between collisional stabilization and H_2 elimination is accurately measured by the experimental PIMS integrated intensity ratios reported in Table 1. However, several factors could produce systematic errors in the ratios, including differences in the reactivity and/or photoionization cross-sections of the primary products. First, the primary products of all four reactions are observed to decrease as a function of hydrocarbon flow, while secondary products appear. The branching ratios in Table 1 are derived from mass spectra collected at low hydrocarbon flows, when primary products dominate. In fact, for the Y + propylene reactions, branching ratios were determined from low-flow mass spectra for which no secondary products were detected. However, for Y + ethylene the secondary reaction is much faster than the primary reaction step. The steady-state concentration of primary products is quickly achieved even at low ethylene flows, and is much smaller than the concentration of secondary products. In this regime, for example, if YC_2D_2 elimination products react less efficiently with C_2D_4 than do stabilized YC_2D_4 complexes, the reported branching ratios will underestimate the fraction of YC_2D_4 complexes produced in the first reaction step. However, we find that all branching ratios are essentially independent of hydrocarbon flow and the different products qualitatively appear to react with similar efficiencies.

Second, it remains possible that the photoionization cross-section and hence the detection efficiency of the products varies, affecting the accuracy of calculated branching ratios. Comparing the total decay of reactant Y^+ signal to the total accumulated product signal at low hydrocarbon flows for which primary products dominate, we estimate that the photoionization cross-sections of the primary products are about a factor of 2 *smaller* than the bare metal. Intuition suggests that the cross-sections of the primary product species, e.g., YC_2H_2 and YC_2H_4, are likely to be more similar and largely unaffected by isotopic substitution. Furthermore, as noted above, the branching ratios do not change even as the laser intensity decreases by a factor of 10. In summary, it remains difficult to quantify the possible impact of secondary reactions and photoionization efficiencies on the reported branching ratios. Ultimately, we find that the statistical rate models can account for the observed Y + ethylene branching ratios, suggesting that the complications described above are minimal.

III. Theoretical: Y + Ethylene

A. Methods. A series of theoretical studies by Blomberg and Siegbahn have identified several stationary points along the Y + C_2H_4 PES, primarily those involved in primary CH bond insertion.[11,12,15,3] Potential minima and transition states were optimized at the Hartree−Fock (HF) level and energies were computed using modified coupled pair functional (MCPF) theory.[11,12,15] Geometry optimizations used double-ζ quality basis sets, while larger sets including diffuse and polarization functions on Y were used for energy calculations. The most recent study repeats these calculations, correcting the MCPF energies for differential effects of configuration interaction using the PCI-80 approximation (Table 2).[3] When possible, energies and structures calculated at the current level of theory will be explicitly compared to those from these earlier studies.

The density functional theory approach used here has been recently described.[10] Briefly, for geometry optimizations of stationary points, potential energy surface scans and intrinsic reaction coordinate (IRC) searches from computed transition states, we combine the B3LYP[21] density functional with the Stuttgart ECP + valence set[39] (triple-ζ quality) for Y and the 6-311++G(d,p) basis set for C and H. We call this hybrid set Stuttgart+6-311++G(d,p) and carry out the electronic structure calculations using the GAUSSIAN-98 (G98) program.[40] All open-shell doublet calculations were performed at the spin-unrestricted level and deviations of the $\langle \hat{S}^2 \rangle$ expectation values from $(3/4)\hbar^2$ were less than 1% for all optimized structures except three, as noted below. After optimization at the level of B3LYP/Stuttgart+6-311++G(d,p), we compute single-point energies for most stationary points using the *m*PW1PW91[22,23] hybrid functional. As found earlier, reoptimization of species at the level of *m*PW1PW91/Stuttgart+6-311++G(d,p) does not significantly lower energies or alter geometries and vibrational frequencies.[10] Electronic stability tests confirmed that the lowest energy solution to the SCF equations was in fact found for each stationary point. IRC following established the connection of all transition states to the expected minima. Unless otherwise indicated, all energies of stationary points are reported relative to ground-state Y (4d^{1}5s^2, ^{2}D) + C_2H_4 reactants, including corrections for zero-point energy (ZPE) effects.

Ideally, the true Y (4d^{1}5s^2, ^{2}D) ground state should be represented by a computed atomic configuration with integral *s* and *d* occupations that correspond to a single Slater determinant with a definite value of *L*.[41,42] However, because we cannot apply symmetry constraints to atoms using the current G98 package, unphysical mixing of the *s* and *d* orbitals can occur, leading to noninteger occupancies. For example, both B3LYP and *m*PW1PW91 give $d_{xz}^{1}\,d_{z^2}^{0.01}\,d_{x^2-y^2}^{0.03}s^{1.96}$ as the lowest energy atomic configuration, and the resulting determinant shows 7% contamination of the nominally doublet wave function. Lying 0.6 kcal/mol above this state, we also find the configuration $d_{z^2}^{0.25}\,d_{x^2-y^2}^{0.75}s^{2}$. Although neither state has integral orbital occupancies, the latter configuration exhibits no spin contamination and we use it to represent the ground-state term Y (4d^{1}5s^2, ^{2}D). We use $d_{xz}^{0.97}\,d_{z^2}^{0.04}\,d_{x^2-y^2}^{0.99}s^{1}$ to represent the excited-state term Y (4d^{2}5s^1, ^{2}F). Again, *d* orbital mixing is unavoidable and the computed value of $\langle\hat{S}^2\rangle$ is 1.75$\hbar^2$, quite different from the pure doublet value of 0.75$\hbar^2$. The calculated excitation energies to this state are 35 and 33 kcal/mol using B3LYP and *m*PW1PW91, respectively; it is 44 kcal/mol experimentally.[43] Both the spin contamination and computed excitation energy to this excited state indicate a contribution of the low-lying term Y (4d^{2}5s^1, ^{4}F), lying 31 kcal/mol above ground-state reactants experimentally.[43] The difficulty of computing accurate atomic state splittings in transition metals using density functional theory is well documented.[42,44]

B. Results. With the electronic wave function constrained to doublet spin multiplicity, we calculate those features of the Y + ethylene PES illustrated in Figure 5. Below the energy level diagram, we include the key structures that illustrate the major atomic motions along the computed reaction paths, while the detailed structural parameters of all reaction intermediates and transition states are given in Figure 6. Table 2 summarizes the energetics of these species, using the Stuttgart+6-311++G-(d,p) basis set with two different density functional methods. Also in Table 2, we collect results from prior theoretical studies. The individual *s* and *d* gross populations and the natural charge of the Y metal center, as determined by a natural bond orbital (NBO) analysis,[45] are given in Table 3. Finally, rotational constants and vibrational frequencies of all stationary points calculated at the level of B3LYP/Stuttgart+6-311++G(d,p) are collected in the Supporting Information to this paper.

An important mechanistic question is whether there exists an energy barrier to the association of the closed-shell s^2 metal and the closed-shell ethylene molecule. Scanning the distance *R* between Y and the midpoint of the CC bond, the B3LYP/Stuttgart+6-311++G(d,p) calculations do locate a small approach barrier to the formation of the long-range Y−C_2H_4 ($^2B_2$) complex (**1a**, described below). The asymmetric entrance channel transition state ^{2}**TS$_{\text{ent}}$** is shown in Figure 6. The transition state is located at very long range, $R = 4.42$ Å, and there is essentially no distortion of the ethylene molecule, especially as compared to structures **1a** and **1b**. The transition vector, also labeled, shows the relative motion of Y and ethylene along the reaction coordinate, *R*. Calculated relative to the lowest energy atomic configuration described above, ($d_{xz}^{1}d_{z^2}^{0.01}\,d_{x^2-y^2}^{0.03}s^{1.96}$), E(^{2}**TS$_{\text{ent}}$**) = +0.29 kcal/mol. However, the atomic configuration with good spin, ($d_{z^2}^{0.25}\,d_{x^2-y^2}^{0.75}s^{2}$), places ^{2}**TS$_{\text{ent}}$** at −0.28 kcal/mol (*below* ground-state reactants). Although our choice of reference ground-state leads to a reported “barrier height” below zero, we include the latter energy in Table 2 since the saddle point is characteristic of the complex forming process. Furthermore, the transition state provides a set of vibrational frequencies and rotational constants for the RRKM model 2 described in Section IV-B. Ultimately, the energy of ^{2}**TS$_{\text{ent}}$** will be adjusted in accord with the experimental results. Finally, the basis set superposition error (BSSE)[46] at ^{2}**TS$_{\text{ent}}$** is small and increases the energy of the transition state by only 0.03 kcal/mol.

Thus at the current level of theory we find that the Y + ethylene entrance channel PES is very flat with essentially no barrier to the approach of the ground-state metal and alkene. As discussed in an earlier theoretical study,[11] Y ultimately binds to ethylene in two distinct modes. The geometry and energy of “long-range” Y−C_2H_4 ($^2B_2$) (**1a**) and “short-range” YC_2H_4 ($^2A_1$) (**1b**) are both described in Figure 6 and Table 2. In the long-range complex **1a**, $R = 2.45$ Å and there is minimal distortion of ethylene ($R_{CC} = 1.39$ Å). In the short-range metallacyclopropane complex **1b**, $R = 2.14$ Å and the ethylene π bond has been essentially broken ($R_{CC} = 1.53$ Å). The geometries of these species are nearly identical to the ones calculated at the HF level.[11] The binding energy of the metallacyclopropane **1b** calculated at the level of B3LYP/Stuttgart+6-311++G(d,p) compares favorably with the energy computed using MCPF+PCI-80 (Table 2).[3] The binding energy of **1a** was not reported in the latter study, but here we find the long-range complex to be substantially bound, located 16 kcal/mol below ground-state reactants. For Y−C_2H_4 ($^2B_2$) (**1a**), the computed value of $\langle\hat{S}^2\rangle$ shows a deviation of 8% from a pure doublet spin description. Using the smaller LANL2DZ basis set, we performed a potential energy surface scan decreasing *R* from the long-range complex minimum, but found no energy barrier in the region of the curve-crossing between **1a** and **1b**.

The bonding mechanism in the two structurally different complexes has been previously outlined by Blomberg et al.[11] and is remarkably similar to the bonding in the analogous long and short-range Zr(ethylene) complexes described in a more recent study.[10] Table 3 gives the electron configuration and natural charge of Y in both **1a** and **1b**. Essentially, the s^2-like long-range complex (**1a**) binds to ethylene using two singly occupied metal−carbon σ-bonds. Two nonbonding electrons occupy an *sd* hybrid that effectively reduces repulsion with the alkene. In the s^1-like metallacyclopropane (**1b**), the metal−carbon bonds are doubly occupied, leaving only one nonbonding electron in the *sd* hybrid.

Next, we confirm the mechanism of primary CH bond insertion by the metallacyclopropane complex (**1b**) implied by earlier work.[12,3] The geometry and energy of the CH insertion transition state ^{2}**TS$_{\text{ins}}$** that connects the metallacyclopropane (**1b**) to an insertion intermediate (**2b**) are described in Figure 6 and Table 2. In ^{2}**TS$_{\text{ins}}$** the short Y−C (2.19 and 2.42 Å) and Y−H (1.95 Å) bond distances and small C2−C1−Y (82°) bond angle indicate the simultaneous interaction of the metal center with the ethylene π-bond and the departing H atom. The CC bond has twisted by nearly 180°, swinging the C2−H1 bond toward the metal center. The substantial lengthening of this bond (1.11 Å) also reflects the presence of stabilizing agostic bonding interactions. The transition vector for the imaginary frequency,

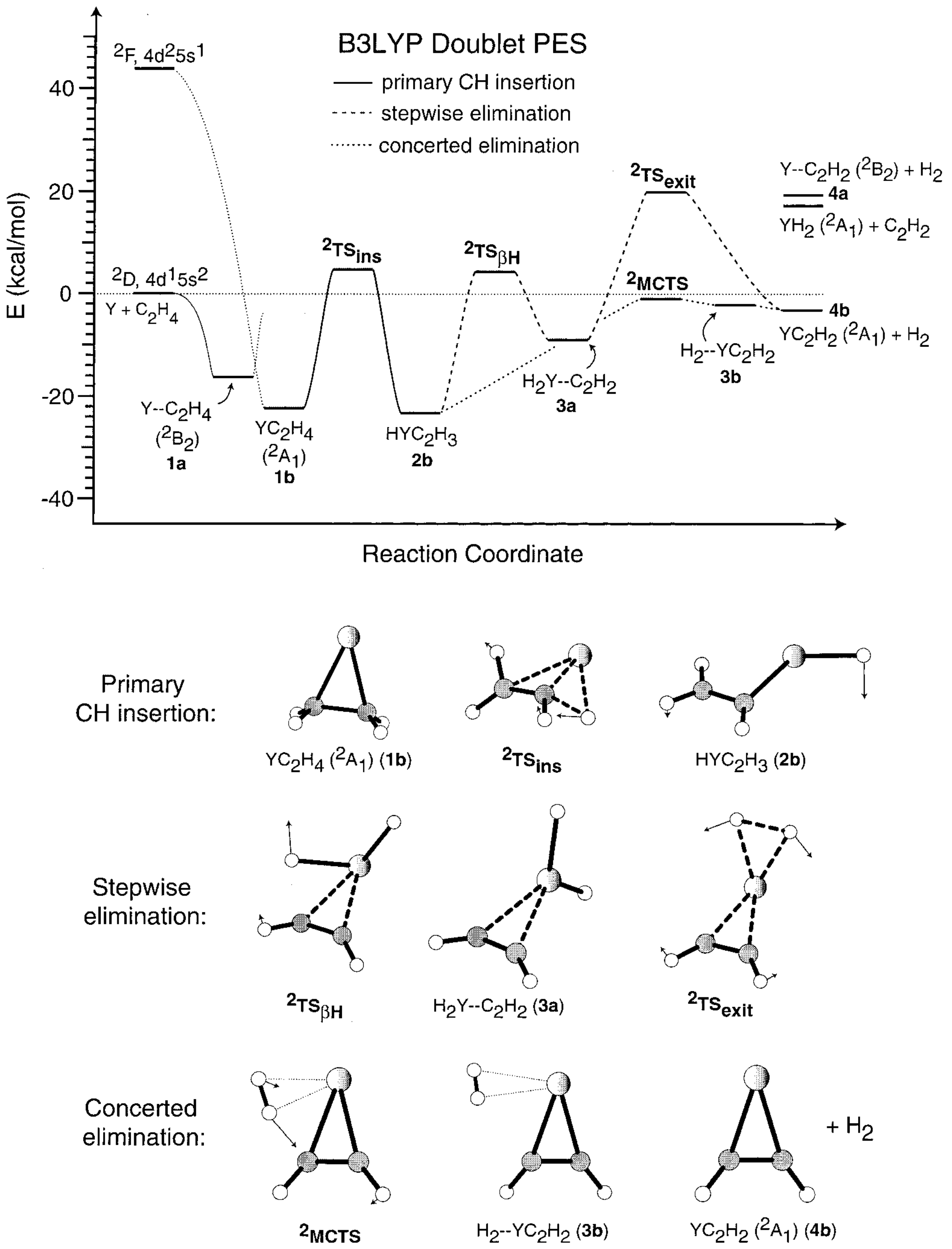

Figure 5. B3LYP/Stuttgart+6-311++G(d,p) reaction path energetics along the doublet PES. All energies measured relative to ground-state Y ($4d^15s^2$, ^2D) + C_2H_4 reactants and corrected for zero-point energy. The location of the $4d^25s^1$, ^2F excited-state term is given by the experimental excitation energy of 44 kcal/mol, not the B3LYP computed value (see text for details).

also labeled in Figure 6, clearly indicates the breaking of the CH bond. The nonplanar structure of ^{2}**TS**$_{\mathbf{ins}}$ is different from the original CH insertion transition state calculated at the HF level, characterized by a bond angle of C2−C1−Y = 128.2°.[12] Carroll et al.[3] do report the energy of a "new and lower" CH insertion transition state than the one previously found[12] but do not describe its geometry.

The resulting planar insertion intermediate HYC_2H_3 (**2b**) is described in Figure 6 and Table 2. Again, agostic interactions account for the small C2−C1−Y bond angle (97°), relatively short Y−C2 distance (2.80 Å), and long C2−H1 bond length (1.11 Å). A potential energy surface scan of the H3−C1−Y−H4 dihedral angle located a nonplanar insertion intermediate **2a** (not shown here) at $\Theta_{H3-C1-Y-H4} = -148°$, with other structural parameters similar to **2b**. Its energy is also included in Table 2. Both **2a** and **2b** appear to be structurally distinct from the insertion intermediate optimized at the HF level, characterized by a C2−C1−Y bond angle of 115.1°.[12] Here, both DFT methods find the nonplanar (**2a**) and planar (**2b**) structures to be nearly isoenergetic, separated by a small barrier of 1 kcal/mol as revealed by the dihedral angle scan. Under all reaction conditions with some 20 kcal/mol of internal energy, rapid conversion between planar and nonplanar HYC_2H_3 will occur. Nonetheless, at the level of B3LYP/Stuttgart+6-311++G-(d,p), IRC scans from ^{2}**TS**$_{\mathbf{ins}}$, ^{2}**TS**$_{\beta\mathbf{H}}$, and ^{2}**MCTS** all led to planar geometries with structural parameters consistent with the insertion intermediate **2b**.

To date, there has been no theoretical investigation of the mechanism of H_2 elimination from the insertion intermediate HYC_2H_3 (**2b**). In our most recent theoretical study of the Zr

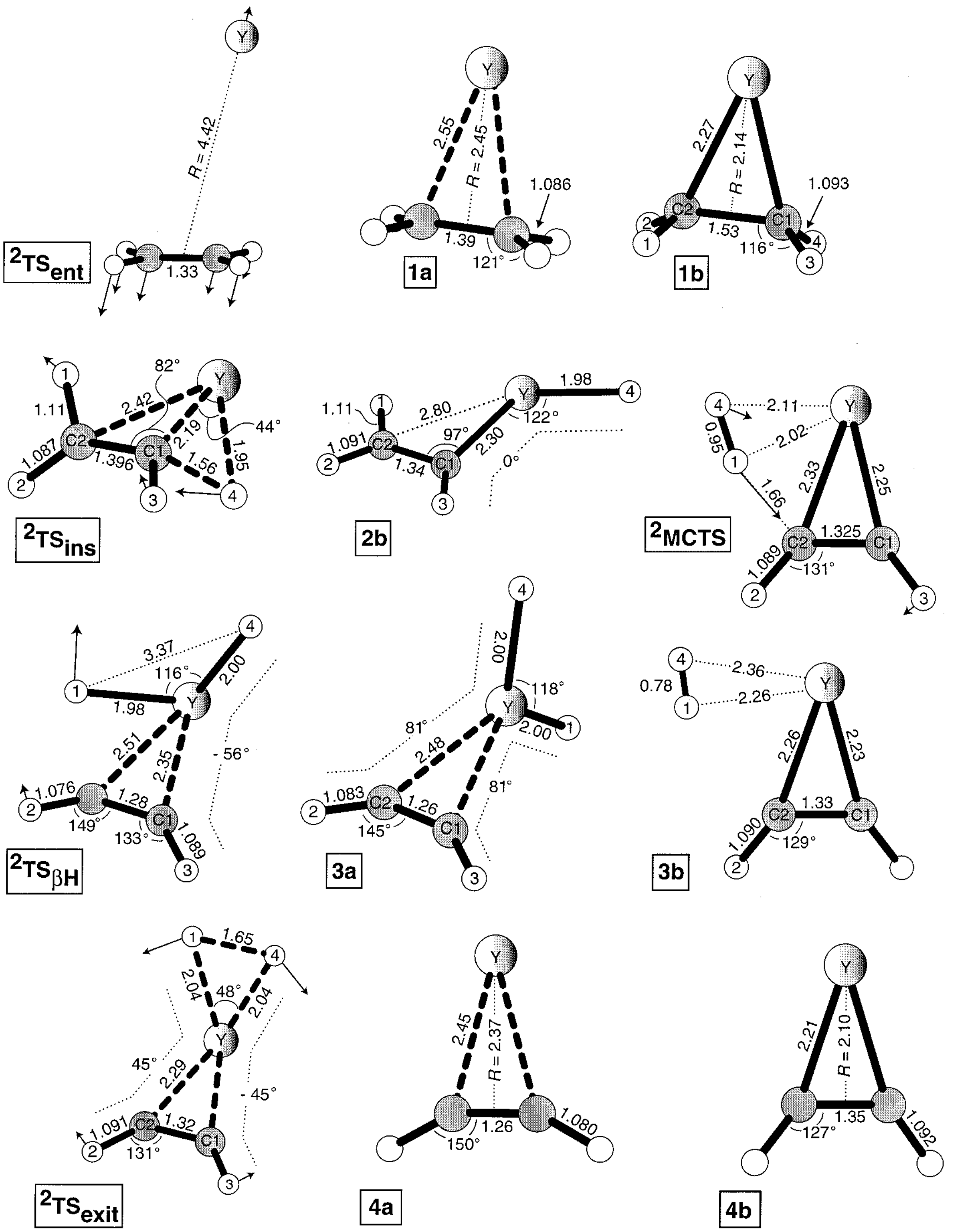

Figure 6. Details of B3LYP/Stuttgart+6-311++G(d,p) optimized geometries of potential minima and transition states for Y + C_2H_4 along the doublet PES. Distances in angstroms; angles in degrees. For each transition state, the transition vector corresponding to the imaginary frequencies is shown.

($4d^25s^2$, ^3F) + ethylene reaction, we identified two reaction paths on the triplet spin surface.[10] The lower energy path involves concerted H_2 elimination from the planar insertion intermediate $HZrC_2H_3$, while the higher energy path involves stepwise H_2 elimination from $HZrC_2H_3$. Similarly, here we find that the Y + ethylene PES also branches from the planar insertion intermediate **2b**. The large-dashed path in Figure 5 follows the stepwise elimination of H_2 via ^{2}**TS**$_{\beta H}$, while the small-dashed path follows the concerted elimination of H_2 via ^{2}**MCTS**. The latter is found to be the lowest energy path to exothermic YC_2H_2 ($^2A_1$) + H_2 products. We find that the key structural and electronic features of intermediates and transition states along the stepwise and concerted paths are very similar to those for the stationary points identified along the analogous paths of the Zr + ethylene triplet PES.

The βH transfer transition state ^{2}**TS**$_{\beta H}$ that carries the planar insertion intermediate (**2b**) to a dihydrido intermediate (**3a**) is described in Figure 6 and Table 2. The labeled transition vector clearly corresponds to the expected β-CH bond stretch. The resulting dihydrido intermediate $H_2Y{-}C_2H_2$ (**3a**), also described in Figure 6 and Table 2, forms strong bonds to hydrogen and weak bonds to acetylene. The geometry and bonding mechanism of the YC_2H_2 unit of the complex are virtually identical to the long-range $Y{-}C_2H_2$ ($^2B_2$) complex (**4a**) described below.

TABLE 3: Natural Populations of Y for Doublet Stationary Points Using B3LYP/Stuttgart+6-311++G(d,p) Theory

species	natural charge[a]	**4d**	**5s**
^{2}**TS**$_{ent}$	+0.007	1.04	1.96
$Y-C_2H_4$ ($^2B_2$) (**1a**)	+0.54	0.63	1.80
YC_2H_4 ($^2A_1$) (**1b**)	+1.11	0.89	0.99
^{2}**TS**$_{ins}$	+1.01	1.02	0.95
nonplanar HYC_2H_3 (**2a**)	+1.23	0.81	0.92
planar HYC_2H_3 (**2b**)	+1.27	0.78	0.90
^{2}**TS**$_{\beta H}$	+1.54	0.96	0.50
2MCTS	+1.08	0.99	0.91
$H_2Y-C_2H_2$ (**3a**)	+1.84	0.79	0.37
$H_2-YC_2H_2$ (**3b**)	+1.08	0.99	0.90
^{2}**TS**$_{exit}$	+1.65	1.13	0.23
$Y-C_2H_2$ ($^2B_2$) (**4a**)	+0.59	0.58	1.81
YC_2H_2 ($^2A_1$) (**4b**)	+1.14	0.85	1.00

[a] The natural charge on Y in units of electrons, as found from an NBO population analysis. In all cases, the 5p population was less than 0.06.

Furthermore, the geometry of the YH_2 unit of the complex is very similar to that calculated for YH_2 ($^2A_1$) products (YH = 1.96 Å and HYH = 114°; structure not shown).

On the lower energy reaction path, a multicenter transition state ^{2}**MCTS** (Table 2) carries the insertion intermediate (**2b**) *directly* to a product-like complex (**3b**). The "late" transition state ^{2}**MCTS** is itself very product-like (Figure 6). The planar geometry and bonding mechanism of the YC_2H_2 unit are similar to the strongly bound YC_2H_2 ($^2A_1$) metallacyclopropene (**4b**) described below. In addition, the Y−H distances are long, 2.11 and 2.02 Å, and the H4−H1 distance is small, 0.95 Å. The NBO analysis[45] reveals substantial donor−acceptor interactions among four center (the two hydrogens, Y, and C1) involving σ_{HH} donation to the metal center and σ_{YC1} back-donation to σ_{HH}*. The transition vector depicted in Figure 6 reveals the concerted motion, the simultaneous β-CH stretch and formation of molecular H_2, that connects the insertion intermediate directly to the precursor complex for H_2 loss (**3b**). The resulting $H_2-YC_2H_2$ complex (**3b**) exhibits strong bonds to acetylene and a weak interaction with molecular H_2 (Figure 6 and Table 2). The Y−H distances have increased to 2.36 and 2.26 Å and the H4−H1 distance has decreased to 0.78 Å, nearly that of the equilibrium bond length in H_2, 0.744 Å. Since ^{2}**MCTS** and $H_2-YC_2H_2$ (**3b**) have similar product-like geometries and bonding mechanisms, it is not surprising that both stationary points lie nearly isoenergetic to the YC_2H_2 ($^2A_1$) + H_2 exit channel. We note that although B3LYP/Stuttgart+6-311++G(d,p) finds $H_2-YC_2H_2$ (**3b**) to be a true minimum, ZPE effects place the complex slightly above YC_2H_2 ($^2A_1$) + H_2 products in energy.

Before discussing the Y + ethylene exit channel PES along the stepwise and concerted reaction paths, we describe the geometry and energetics of the YC_2H_2 + H_2 products themselves. As for ethylene, we find that Y binds to acetylene in two distinct modes. The geometry and energy of the $Y-C_2H_2$ ($^2B_2$) complex (**4a**) are described in Figure 6 and Table 2. Like the $Y-C_2H_4$ ($^2B_2$) complex (**1a**), **4a** binds at a long range. No similar long-range $Y-C_2H_2$ complex has been reported in the literature. The geometry and energy of the YC_2H_2 ($^2A_1$) (**4b**) complex are also described in Figure 6 and Table 2. This short-range complex is a true metallacyclopropene, since the acetylene triple bond has been effectively broken. The geometry of **4b** is similar to the structure reported earlier, optimized at the HF level.[15] We calculate the binding energy of **4a** to be only 20.9 kcal/mol, and as for the long-range complex **1a**, there is some spin contamination (6%) of the B3LYP determinant. We compute a binding energy of 43.4 kcal/mol for **4b**, in good agreement with the binding energy of 48.6 kcal/mol calculated at the MCPF level.[3] Finally, the bonding mechanisms in the acetylene complexes parallel those already described for the ethylene complexes. The additional interaction of the out-of-plane π orbital with the metal *d* orbitals accounts for the very strong metal−acetylene binding as discussed earlier.[15,10]

Next, we directly explore the connection of **3a** and **3b** to products following either the stepwise H_2 elimination reaction path or the concerted H_2 elimination reaction path. Along the former path, we locate a large exit barrier ^{2}**TS**$_{\mathbf{exit}}$ of +23 kcal/mol that connects the dihydrido intermediate $H_2Y-C_2H_2$ (**3a**) to products (Figure 6 and Table 2). The transition vectors, also labeled in Figure 6, indicate the H1−Y−H4 bond-angle stretch and reorientation of the acetylene group that accompanies the conversion of **3a** to products. In contrast, we find no exit channel barrier along the concerted H_2 elimination reaction path. Starting from the $H_2-YC_2H_2$ (**3b**) minimum, we compute the energy while scanning the distance between Y and H4, optimizing the geometry at each fixed value of Y−H4. At the level of B3LYP/Stuttgart+6-311++G(d,p), we find that **3b** dissociates smoothly to YC_2H_2 ($^2A_1$) + H_2 products with no barrier.

Finally, we note that the two DFT methods differ substantially in their predictions of stationary point energetics along the Y + ethylene PES (Table 2). Compared to B3LYP, *m*PW1PW91 increases binding energies and lowers transition states relative to ground-state reactants by about 5 kcal/mol on average. This is quite similar to the performance of the same functionals on the Zr + ethylene system.[10] Next we use a statistical rate model to assess the relative performance of the different theories in explaining the behavior of the Y + ethylene reaction.

IV. Statistical Rate Model: Y + Ethylene

The electronic structure calculations presented in Section III-B provide the necessary input for RRKM[28,29] rate calculations along the Y + ethylene PES. Here, we build a statistical model of the decay of long-lived metallacyclopropane (**1b**) complexes. The energies of key intermediates and transition states will be adjusted to fit the collection of experimental data (Table 1), providing both a quantitative mechanistic picture of primary CH bond insertion and a critical test of the different levels of theory (Table 2). With only the doublet surface important, Y + ethylene provides a cleaner test of DFT than Zr + ethylene, for which both a singlet and a triplet surface are probably involved in the dynamics.

The statistical rate model employed here differs from previous work[6] and will be described in detail below. In the model, long-lived collision complexes are formed at a rate determined by the Lennard−Jones rate constant k_{LJ} and details of the long-range interactions. Complexes (**1b**) then decay into three parallel channels, dissociation back to reactants (k_{diss}), stabilization by a third-body collision into the strongly bound metallacyclopropane well (k_Q[He]) and insertion into a CH bond (k_{ins}). We note that the PIMS data determine the mass, not the structure, of detected products. However, from RRKM theory we expect that stabilized complexes will be dominated by the species **1b**, due to the large density of rovibrational states. Although theory identifies two reaction paths emanating from HYC_2H_3 (**2b**), the low-energy ^{2}**MCTS** ensures that the concerted mechanism dominates and that all insertion intermediates will go on to eliminate H_2, rather than become trapped in **2b** (Figure 5).

As before, our model calculations are somewhat oversimplified; they are intended to demonstrate that a range of plausible parameters can explain all of the data. The connection between the model and the experimental data is made via the microcanonical rate constant:

$$k(\bar{E}) = \sum_{J=0}^{J_{\max}} P(J)k(\bar{E},J) = Ak_{\mathrm{LJ}} \sum_{J=0}^{J_{\max}} P(J)\frac{k_{\mathrm{ins}}(\bar{E},J) + k_{\mathrm{Q}}[\mathrm{He}]}{k_{\mathrm{ins}}(\bar{E},J) + k_{\mathrm{diss}}(\bar{E},J) + k_{\mathrm{Q}}[\mathrm{He}]} \qquad (5)$$

Here $\bar{E}$ is the mean total energy including $\bar{E}_t$, the average kinetic energy of those thermal collisions that can surmount the assumed entrance channel barrier for zero-impact parameter collisions, and the mean ethylene vibrational energy. Notably, we do not explicitly average eq 5 over a 300 K Boltzmann distribution of energies, but instead carry out the microcanonical rate calculations using the average energies, as defined above. The total angular momentum is given by J with a distribution $P(J) = 2J/J_{\max}^2$, where $J_{\max}$ is the largest value of J for the metallacyclopropane (**1b**) complexes. We assume there is no ethylene rotational energy ($\vec{j} = 0$) contributed to the reaction rate so that $\vec{J} = \vec{l}$, where l is the orbital angular momentum of the collision. The total rate of bimolecular collisions at 300 K is given by k_{LJ}, further described below. However, not all collisions are "successful." We define A as the reaction inefficiency factor, i.e., the fraction of Lennard–Jones collisions that actually gain access to the deep metallacyclopropane (**1b**) well. Possible origins of reaction inefficiency will be discussed in detail below.

The absence or presence of an approach barrier to the formation of metallacyclopropane (**1b**) complexes distinguishes two rate models, one for which $E(^2\mathbf{TS_{ent}}) = 0$ kcal/mol (model 1) and one for which $E(^2\mathbf{TS_{ent}}) > 0$ kcal/mol (model 2). Accordingly, each model ascribes very different meanings to the inefficiency factor A. In model 1, we attribute a portion of the overall reaction inefficiency to nonadiabatic or steric effects; neither effect is easy to estimate a priori. Thus, A simply represents the factor required to force the calculated Y + ethylene rate constant into accord with the measured bulk kinetics value. In model 2, A includes two factors, the fraction of the 300 K Boltzmann distribution with kinetic energy above the approach barrier energy threshold for $l = 0$, including differential zero-point energy effects; and the fraction of those sufficiently energetic collisions that can surmount the centrifugal barrier atop $^2\mathbf{TS_{ent}}$.

Each unimolecular rate constant in eq 5 is computed from the usual RRKM expression by a program based on the work of Yi et al.[24] We explore how the barrier heights for $^2\mathbf{TS_{ent}}$ and $^2\mathbf{TS_{ins}}$ and the binding energy of YC_2H_4 ($^2A_1$) (**1b**) impact the microcanonical rate constants k_{diss} and k_{ins} and what combination of stationary point energies best explains the experimental data. Although both B3LYP and *m*PW1PW91 compute the energy of $^2\mathbf{TS_{ent}}$ to lie slightly below ground-state reactants, we test approach barrier heights that range from 0 to 3 kcal/mol. Correspondingly, the treatment of the entrance channel transition state varies from loose to tight. In all calculations, the transition state $^2\mathbf{TS_{ins}}$ is modeled as tight. We use the B3LYP/Stuttgart+6-311++G(d,p) rotational constants and vibrational frequencies for all three stationary points, collected in the Supporting Information to this paper.

In the flow tube at 0.8 Torr total pressure, quenching occurs via collisions with the buffer gas (mostly He) at a rate $k_{\mathrm{Q}}[\mathrm{He}] \approx 3 \times 10^6$ s^{-1}. This estimate uses $k_{\mathrm{Q}} = 1 \times 10^{-10}$ cm^3 s^{-1}, about 5 times smaller than the hard-spheres collision rate, because lack of vibrational or rotational degrees of freedom make He a rather inefficient quencher.[3] In our rate model, we allow k_{Q} to vary by no more than a factor of 2 about this value, placing $k_{\mathrm{Q}}[\mathrm{He}]$ within the range 1.5–6.0 × 10^6 s^{-1}.

In the absence of an approach barrier (model 1), we compute the total rate of bimolecular collisions as $k_{\mathrm{LJ}} = \pi b^2_{\max}\bar{v} = \pi l^2_{\max}/\mu^2\bar{v}$. Here, $l_{\max}$ is the largest value of orbital angular momentum that can penetrate the maximum of the effective potential, which includes an estimated long-range attraction $-C_6/R^6$;[47] μ is the reduced mass of the collision pair; and $\bar{v}$ is the relative velocity at $\bar{E}_t$, the mean collision energy at 300 K. In such a model, $\bar{E}_t = 0.9$ kcal/mol and $l_{\max} = 123$, giving $k_{\mathrm{LJ}} = 7.74 \times 10^{-10}$ cm^3 s^{-1} for Y + C_2H_4. By this measure, the Y + C_2H_4 reaction efficiency at room temperature, estimated as $k_{\mathrm{H}}/k_{\mathrm{LJ}}$, is only 1%.

Model 2 assumes the presence of an approach barrier of variable magnitude. We then carry out microcanonical RRKM rate calculations for which $\bar{E}'_t$ is now defined as the mean kinetic energy of *that fraction of collisions with energy above threshold*, given a particular energy of $^2\mathbf{TS_{ent}}$. The inclusion of an approach barrier further constrains the range of orbital angular momenta that can surmount the centrifugal barrier atop $^2\mathbf{TS_{ent}}$ to reach the deep metallacyclopropane (**1b**) well. We calculate the rate of association over $^2\mathbf{TS_{ent}}$ from $k_f\ \pi l'^2_{\max}/\mu^2\bar{v}'$ where $\bar{v}'$ is the relative velocity corresponding to $\bar{E}'_t$ and $l'_t = \mu\bar{v}'b'_{\max}$. For example, when $E(^2\mathbf{TS_{ent}}) = 2$ kcal/mol, $\bar{E}'_t = 2.66$ kcal/mol and $l'_{max} = 77$, yielding $k_f = 1.46 \times 10^{-10}$ cm^3 s^{-1} for Y + C_2H_4. In this scenario, only a small fraction of collisions (0.079) have sufficient energy to surmount the approach barrier and angular momentum effects further reduce efficiency. Thus, the rate of formation of long-lived complexes becomes $0.079k_f \equiv Ak_{\mathrm{LJ}}$, yielding an effective $A = 0.015$.

The Y + ethylene experimental data that constrain the possible output of the statistical rate model (Table 1) include the bimolecular rate constant $k = 7.4 \pm 2.2 \times 10^{-12}$ cm^3 s^{-1} and the kinetic isotope effect $k_{\mathrm{H}}/k_{\mathrm{D}} = 1.75 \pm 0.12$. In addition, we equate the experimental PIMS intensity ratios to the branching ratio of stabilized complexes to elimination products, i.e., to $k_{\mathrm{Q}}[\mathrm{He}]/k_{\mathrm{ins}}$ in the rate model. Thus, $k_{\mathrm{Q}}[\mathrm{He}]/k_{\mathrm{ins}} \leq 0.10 \pm 0.03$ for Y + C_2H_4 and $k_{\mathrm{Q}}[\mathrm{He}]/k_{\mathrm{ins}} = 0.33 \pm 0.09$ for Y + C_2D_4. Possible experimental complications were discussed in Section II-B.

A. Model 1: No Entrance Channel Barrier. The electronic structure calculations described above find no energy barrier to the approach of Y and ethylene along the adiabatic entrance channel. Thus, our first model assumes that metallacyclopropane complexes (**1b**) dissociate over a loose, orbiting transition state, whose placement is defined as the maximum in the effective potential for Y + ethylene collisions, as usual.[28,29] The results using the *m*PW1PW91 binding energy for **1b** (−31 kcal/mol), the estimate $k_{\mathrm{Q}}[\mathrm{He}] = 3 \times 10^6$ s^{-1}, and a variety of assumptions about the energy of $^2\mathbf{TS_{ins}}$ are collected in Table 4. Superscripts H or D on rate constants refer to the reaction Y + C_2H_4 or Y + C_2D_4, respectively. Vibrational frequencies, rotational constants and other input parameters are suitably modified for calculations of Y + C_2D_4. In Table 4, we note that the values of k_{H} and k_{D} calculated from eq 5 use $A = 1$, so that the predictions of the model are made readily apparent. The factor A will later be adjusted to fit the bulk kinetics rate constant (Table 5), given the model parameters found to best fit the isotope effect and product branching ratios.

Equation 5 reveals that the experimentally observed rate constant and kinetic isotope effect are determined by the competition between the rates of dissociation, stabilization and insertion. When k_{diss} dominates both $k_{\mathrm{Q}}[\mathrm{He}]$ and k_{ins}, the model

TABLE 4: RRKM Rate Constants for Model 1: No Entrance Channel Barrier[a]

	$E(^2\mathbf{TS_{ins}})$ (kcal/mol)[b]				
rate or ratio	−1	−2	−3	−4	−5
$k_{ins}^{H}(10^8\ s^{-1})$	0.019	0.071	0.216	0.575	1.400
$k_{ins}^{D}(10^8\ s^{-1})$	0.0005	0.003	0.014	0.047	0.140
k_{ins}^{H}/k_{ins}^{D}	38	24	15	12	10
$k_H(10^{-12}\ cm^3\ s^{-1})$	18.3	36.0	75.1	143	242
$k_D(10^{-12}\ cm^3\ s^{-1})$	35.8	39.5	52.4	85.4	148
k_H/k_D	0.51	0.91	1.43	1.68	1.64
$k_H[He]k_{ins}^{H}$	1.56	0.42	0.14	0.05	0.02
$k_Q[He]k_{ins}^{D}$	61.9	9.58	2.22	0.64	0.21

[a] Calculations use $E(\mathbf{1b}) = -31$ kcal/mol and $k_Q[He] = 3 \times 10^6$ s^{-1}. The factor $A = 1$ and will be adjusted later (Table 5). In the absence of an approach barrier, $\bar{E}_t = 0.9$ kcal/mol, and the estimated association rates for Y + C_2H_4 and Y + C_2D_4 are: $k_{LJ}^{H} = 7.74 \times 10^{-10}$ $cm^3\ s^{-1}$ and $k_{LJ}^{D} = 7.36 \times 10^{-10}$ $cm^3\ s^{-1}$. Assuming metallacyclopropane complexes dissociate over a loose, orbiting transition state, the computed complex dissociation rates are $k_{diss}^{H} = 2.24 \times 10^8\ s^{-1}$ and $k_{diss}^{D} = 6.33 \times 10^7\ s^{-1}$. [b] Placement of $^2\mathbf{TS_{ins}}$ for each column of RRKM calculations. The *m*PW1PW91 functional gives $^2\mathbf{TS_{ins}}$ at −3 kcal/mol relative to Y + C_2H_4 reactants.

TABLE 5: Rate Constants, Isotope Effects, and Branching Ratios as Determined by Experiment and RRKM Models 1 and 2

rate or ratio	experiment[a]	model 1[b]	model 2[c]
$k_H(10^{-12}\ cm^3\ s^{-1})$	7.4 ± 0.3	7.15	9.7
$k_D(10^{-12}\ cm^3\ s^{-1})$	4.2 ± 0.12	4.26	6.0
k_H/k_D	1.75 ± 0.12	1.68	1.62
$k_D[He]k_{ins}^{H}$	≤0.10 ± 0.03	0.05	0.015
$k_D[He]k_{ins}^{D}$	0.33 ± 0.09	0.64	0.241

[a] Values as determined by the present work; see text and Table 1 for details. Error estimates refer to the precision of the experiments. Absolute accuracy of k_H and k_D are ±30%. [b] Values as determined by model 1 which uses $A = 0.05$, $E(\mathbf{1b}) = -31$ kcal/mol, $E(^2\mathbf{TS_{ins}}) = -4$ kcal/mol and $k_Q[He] = 3 \times 10^6\ s^{-1}$; see text and Table 4 for details. [c] Values as determined by model 2 which uses $E(^2\mathbf{TS_{ent}}) = 2$ kcal/mol ($A = 0.015$), $E(\mathbf{1b}) = -26$ kcal/mol, $E(^2\mathbf{TS_{ins}}) = -1$ kcal/mol and $k_Q[He] = 1.5 \times 10^6\ s^{-1}$; see text and Table 6 for details.

TABLE 6: RRKM Rate Constants for Model 2: Non-Zero Entrance Channel Barrier[a]

	$E(^2\mathbf{TS_{ins}})$ (kcal/mol)[b]				
rate or ratio	0	−1	−2	−3	−4
$k_{ins}^{H}(10^8\ s^{-1})$	0.333	0.987	2.56	5.99	13.0
$k_{ins}^{D}(10^8\ s^{-1})$	0.013	0.062	0.218	0.645	1.69
k_{ins}^{H}/k_{ins}^{D}	26	16	12	9	8
$k_H(10^{-12}\ cm^3\ s^{-1})$	7.2	9.7	10.8	11.3	11.5
$k_D(10^{-12}\ cm^3\ s^{-1})$	3.4	6.0	9.1	10.9	11.7
k_H/k_D	2.1	1.62	1.19	1.03	0.98
$k_Q[He]/k_{ins}^{H}$	0.04	0.015	0.006	0.003	0.001
$k_Q[He]/k_{ins}^{D}$	1.14	0.241	0.069	0.023	0.009

[a] Calculations use $E(^2\mathbf{TS_{ent}}) = 2$ kcal/mol, $E(\mathbf{1b}) = -26$ kcal/mol, and $k_Q[He] = 1.5 \times 10^6\ s^{-1}$. Here, $\bar{E}_t = 2.66$ kcal/mol, and *A* becomes 0.015 and 0.016 for Y + C_2H_4 and Y + C_2D_4, respectively (see text for details). Assuming metallacyclopropane complexes dissociate over the tight transition state $^2\mathbf{TS_{ent}}$, the computed complex dissociation rates are $k_{diss}^{H} = 2.06 \times 10^7\ s^{-1}$ and $k_{diss}^{D} = 7.21 \times 10^6\ s^{-1}$. [b] Placement of $^2\mathbf{TS_{ins}}$ for each column of RRKM calculations. The *m*PW1PW91 functional gives $^2\mathbf{TS_{ins}}$ at −3 kcal/mol relative to Y + C_2H_4 reactants.

predicts a relatively inefficient reaction, since a large fraction of complexes dissociate; and an inverse isotope effect, since YC_2D_4 complexes are longer lived. As $^2\mathbf{TS_{ins}}$ is lowered, the rate of insertion and the overall reaction rate rapidly increase. When $^2\mathbf{TS_{ins}}$ lies at least 11 kcal/mol below reactants (data not shown), k_{ins} dominates $k_Q[He]$ and k_{diss}. The model then predicts that the overall reaction rate k_H approaches the rate of bimolecular collisions k_{LJ}^{H} and the deuterium isotope effect disappears, with $k_{LJ}^{H}/k_{LJ}^{D} = 1.05$. In this limit, essentially all complexes go on to insert into a CH bond of ethylene and a negligible fraction become stabilized into the deep metallacyclopropane (**1b**) well, since $k_{ins} \gg k_Q[He]$.

The experimental data rule out either extreme, dominant dissociation or dominant insertion. Furthermore, the observation of a small normal isotope effect, the absence of stabilized YC_2H_4 complexes within experimental sensitivity, and the small measured fraction of stabilized YC_2D_4 complexes constrain the magnitude of $^2\mathbf{TS_{ins}}$. When $E(^2\mathbf{TS_{ins}}) = -4$ kcal/mol the model comfortably agrees with these data. The overall reaction rate is much less sensitive to the binding energy of **1b** and the precise value of $k_Q[He]$; instead, these parameters primarily impact the isotope effect and branching ratios. Given $E(^2\mathbf{TS_{ins}}) = -4$ kcal/mol, minor adjustments to the other parameters can tune the ratios toward even better agreement with the data. For example, if we decrease the binding energy of **1b** by 2 kcal/mol, k_H/k_D increases to 1.94, while the branching ratios $k_Q[He]/k_{ins}$ decrease to 0.03 and 0.35 for Y + C_2H_4 and Y + C_2D_4, respectively. Alternatively, if $k_Q[He]$ is decreased to $2.3 \times 10^6\ s^{-1}$, k_H/k_D becomes 1.80 while the branching ratios are 0.04 and 0.49 for Y + C_2H_4 and Y + C_2D_4, respectively.

Table 4 also shows that for the energies of **1b** and $^2\mathbf{TS_{ins}}$ that approximately reproduce the observed isotope effect and product branching data, the overall reaction rate k_H is about 19 times faster than experiment (Table 1). As mentioned earlier, in this model, we must attribute the overall reaction inefficiency to either nonadiabatic or steric effects. Both would limit the fraction *A* of Y + ethylene collisions that gain access to the deep metallacyclopropane (**1b**) well as discussed further below. Specifically, to match the 300 K bulk rate constant when $E(^2\mathbf{TS_{ins}}) = -4$ kcal/mol, we require that $A \approx 0.05$.

Table 5 directly compares representative "good fit" results from model 1 to the available experimental data. To summarize, for $A \approx 0.05$, $E(\mathbf{1b}) = -31 \pm 2$ kcal/mol, $E(^2\mathbf{TS_{ins}}) = -4 \pm 1$ kcal/mol, and for reasonable values of $k_Q[He]$, model 1 can explain all of the Y + ethylene data. Furthermore, since *m*PW1PW91 does not find an approach barrier and places **1b** and $^2\mathbf{TS_{ins}}$ at −31 and −3 kcal/mol, respectively, this functional yields energies consistent with experiment within the limitations of our approximate rate model. In contrast, the **1b** and $^2\mathbf{TS_{ins}}$ energies of −22.3 and +4.8 kcal/mol from B3LYP are much too high.

B. Model 2: Non-Zero Entrance Channel Barrier. Given the modest isotope effect and the small fraction of stabilized complexes, the statistical rate modeling thus far shows clearly that the 1% efficiency of the Y + ethylene reaction is only partly due to the failure of metallacyclopropane (**1b**) complexes to insert in a CH bond of ethylene. Model 1 attributes the bulk of the reaction efficiency to nonadiabatic or steric effects. Next we explore model 2, for which a real energy barrier in the entrance channel limits the fraction of collisions that gain access to the deep metallacyclopropane (**1b**) well. Thus we assume that the complexes dissociate over the tight transition state $^2\mathbf{TS_{ent}}$, whose energy is allowed to vary from 0 to 3 kcal/mol.

Representative results for $E(^2\mathbf{TS_{ent}}) = 2$ kcal/mol are collected in Table 6, using $E(\mathbf{1b}) = -26$ kcal/mol, the estimate $k_Q[He] = 1.5 \times 10^6\ s^{-1}$, and a variety of assumptions about the energy of $^2\mathbf{TS_{ins}}$. Aside from reducing the number of successful

Y−ethylene collisions, the primary effect of the model with an approach barrier is to dramatically decrease k_{diss} at a given collision energy. Consequently, for relatively large values of $\mathbf{^2TS_{ins}}$, k_{ins} dominates k_{diss} and k_Q[He], resulting in the absence of an isotope effect and a small fraction of stabilized complexes, as explained above. Although almost all complexes insert when $\mathbf{^2TS_{ins}}$ lies at −3 kcal/mol, only a small fraction (0.015) of collisions are able to surmount the association barrier. When $E(\mathbf{^2TS_{ent}}) = 2$ kcal/mol, $E(\mathbf{1b}) = -26$ kcal/mol and $E(\mathbf{^2TS_{ins}}) = -1$ kcal/mol, the model approximately matches the experimental reaction rate, isotope effect and branching ratios. Within the assumptions of model 2, the energy of $\mathbf{^2TS_{ent}}$ is well constrained by the 300 K bulk rate constant. Additional RRKM calculations considered other combinations of **1b**, $\mathbf{^2TS_{ins}}$, and k_Q[He]. Such changes either produce less acceptable agreement with the experimental data, deviate further from the electronic structure results, or conflict with our expectations about k_Q[He].

Predictions of model 2 are compared directly with experiment in Table 5. Model 2 places the best-fit values of $\mathbf{^2TS_{ent}}$, **1b**, and $\mathbf{^2TS_{ins}}$ at energies 3.4, 5.0, and 2.0 kcal/mol *higher* than those predicted by *m*PW1PW91. These adjustments are larger than those called for by model 1. The required adjustments remain substantial for the B3LYP functional, which computes $\mathbf{^2TS_{ent}}$, **1b**, and $\mathbf{^2TS_{ins}}$ to be 2.3, 3.7, and 5.8 kcal/mol too high relative to the values favored by model 2. As discussed below, we favor model 1 since it more readily fits the experimental data and requires only minor adjustments to the *m*PW1PW91 electronic structure results, which required only small adjustments for the Zr + ethylene reaction as well.[10]

V. Discussion

Before discussing the impact of the statistical rate modeling on our understanding of the Y ($4d^15s^2$, ^2D) + ethylene reaction, we compare the new theoretical results to our recent findings in the related Zr ($4d^25s^2$, ^3F) + ethylene system.[10] In neither case does DFT in its B3LYP or *m*PW1PW91 form find any substantial barrier to the formation of a long-range metal−ethylene complex along the adiabatic entrance channel, despite the fact that the reactions exhibit 300 K efficiencies of only 1% and 7%, respectively.[2,5] Along both the doublet Y + ethylene PES and the triplet Zr + ethylene PES, two distinct H_2 elimination paths have been found, a stepwise and a concerted path. For both reactions, regardless of the DFT method employed, a high-energy exit barrier (here, $\mathbf{^2TS_{exit}}$) precludes H_2 elimination via the stepwise path at low collision energies. Along the low-energy path, the strongly bound insertion intermediate (here, **2b**) rearranges to H_2 elimination products in a concerted fashion via a multicenter transition state (here, $\mathbf{^2MCTS}$).

Theory has also identified key MCTSs involved in the H_2 elimination mechanisms of Fe^+ ($3d^64s^1$, ^6D), Co^+ ($3d^8$, ^3F) and Ni^+ ($3d^9$, ^2D) with small alkanes, and of Pt ($5d^96s^1$, ^3D) with methane.[24,27,48−51] Apparently, the MCTSs are important when the metal center lacks sufficient bonding capacity to form covalent bonds to both hydrogen atoms and to the remaining alkene or alkyne. For example, in Zr + ethylene, the Zr ($4d^25s^2$, ^3F) atom has four valence electrons, but they are triplet coupled. Only for Zr in its singlet spin state are the reaction intermediates and transition states along the stepwise H_2 elimination path favorable in energy.[3,10] In fact, the excited singlet spin surface is expected to play an important role in the behavior of the Zr + ethylene system, competing with primary CH insertion and concerted H_2 elimination on the triplet surface, as argued recently.[10] In the present study, because the Y ($4d^15s^2$, ^2D) atom has only three valence electrons, the lowest energy pathway must again involve the concerted elimination of H_2, now via $\mathbf{^2MCTS}$ on the doublet PES.

Although the B3LYP and *m*PW1PW91 functionals predict very different stationary point energies along the Y + ethylene PES, the statistical rate models described above help to independently constrain the energetics of the key reaction intermediates and transition states involved in primary CH bond insertion. The small normal isotope effect, the absence of stabilized YC_2H_4 complexes, and the small fraction of stabilized YC_2D_4 complexes indicate that insertion competes with dissociation, i.e., neither process can dominate. The comparison of well-tuned models 1 and 2 (details above) with experiment (Table 5) shows that the parameters preferred by model 1 are very similar to the *m*PW1PW91 results. Larger, upward adjustments to the *m*PW1PW91 energies are demanded by model 2. Regardless of which model is chosen, it is clear that $\mathbf{^2TS_{ins}}$ must lie 1−4 kcal/mol *below* ground-state reactants. This is 6−9 kcal/mol *lower* than the B3LYP value, but within ±2 kcal/mol of the *m*PW1PW91 value, depending on the model. There is by now abundant evidence that B3LYP consistently overestimates the energy of key transition states by a similar amount in many related transition metal−hydrocarbon systems.[24−27]

The remaining subtle issue involves the origin of the room-temperature reaction efficiency, which is about 1% for Y + C_2H_4 and increases to about 16% for Y + C_3H_6. For Y + C_2H_4, the reaction efficiency is a product of two probabilities: the fraction of collisions that reach the deep metallacyclopropane well (**1b**) times the fraction of those complexes that are collisionally stabilized or eliminate H_2 rather than dissociating back to reactants. The former fraction is given by the inefficiency factor *A* in eq 5, attributed to nonadiabatic effects or steric effects in model 1 and to a small entrance channel barrier and its associated angular momentum effects in model 2. The latter fraction is determined by the *J*-averaged model ratio (k_{ins} + k_Q[He])/(k_{ins} + k_Q[He] + k_{diss}), which is quite sensitive to isotope effect and product branching ratios. For this discussion, call the latter fraction B. From the calculations in Table 5, for model 1, $A = 0.05$ and $B = 0.185$. For model 2, $A = 0.015$ and $B = 0.841$. The calculated reaction rates k_H are then given by ABk_{LJ} and are listed in Table 5; both models are in reasonable agreement with the experimentally determined k_H. However, the two models differ substantially in their partitioning of the reaction inefficiency. Additional experimental data would further constrain the RRKM calculations, possibly ruling out one model or the other. For example, at high pressures the fraction B will be driven toward unity as k_Q[He] dominates both k_{ins} and k_{diss}. In this regime, because all collision complexes are stabilized, the bulk kinetics measures the fraction of complexes that have gained access to the metallacyclopropane (**1b**) well. With B = 1, model 1 and model 2 predict overall reaction rates that differ by more than a factor of 3.

We can suggest several effects that may contribute to reaction inefficiency. The first is a small entrance channel barrier, which provides both an energy cutoff and an angular momentum cutoff to limit the rate of formation of metallacyclopropane complexes, as described above. We might expect the entrance channel barrier height to be similar for ethylene and propylene, so it is not easy to understand the far greater reactivity of Y + propylene in this context. The second is a steric effect, meaning that not all Y + alkene approach angles are energetically favorable. Presumably the extra methyl group on propylene presents *greater* steric difficulty to an incoming Y atom, in disagreement with the greater reaction efficiency for propylene.

The third effect involves the fraction of collisions that find the attractive potential surface rather than one of the several repulsive surfaces emanating from Y + alkene reactants. With one unpaired *d* electron, the Y ($4d^15s^2$, ^2D) reactant atom has 5-fold spatial degeneracy corresponding to occupancy of the five different *d* orbitals. Naively, only one in five collisions will find the attractive potential for which the good acceptor orbital d_{yz} is occupied. Nonadiabatic transitions at long range in the entrance channel may alter this fraction, and, in fact, Y + propylene may be more successful at finding the attractive potential than Y + ethylene. The reason is that the nonadiabatic process at long range is analogous to a nonradiative transition between nearly degenerate electronic states. The larger density of rovibrational states for Y−propylene may enhance transitions to the more stable potential as the collision proceeds. Finally, Y + propylene could be more efficient than Y + ethylene because additional reaction channels involving CC insertion may contribute, or the presence of the methyl group may significantly stabilize $^2\mathbf{TS_{ins}}$, allowing a greater fraction of complexes to eliminate rather than dissociate.

The two rate models are extreme cases that attribute the reaction inefficiency either entirely to nonadiabatic and/or steric effects (model 1) or entirely to a small barrier at $^2\mathbf{TS_{ent}}$ (model 2). Of course a combination of factors could come into play. However, we tend to favor model 1 (no approach barrier) over model 2 in part because it more comfortably fits the experimental data and in part because theory consistently fails to find such an entrance channel barrier. Although the prevailing view has been that repulsive long-range forces arise from the interaction of closed-shell s^2 metal atoms with close-shell alkenes, density functional theory does not find a barrier along the adiabatic entrance channel for Y ($4d^15s^2$, ^2D) + ethylene. From a theoretical point of view, *m*PW1PW91 may provide a better model of such long-range interactions than B3LYP. The *m*PW1PW91 functional was specifically designed to correct deficiencies in the B3LYP functional, which has been shown to *underestimate* the attractive interactions of weakly bound systems.[22,23,17] If theory is correct, then we must attribute the overall Y + ethylene reaction inefficiency primarily to nonadiabatic and/or steric effects, as described above.

The close agreement between the *m*PW1PW91 energetics and the experimental data, as revealed by model 1, further supports the viability of this hybrid density functional. Increased confidence in the *m*PW1PW91 functional in turn strengthens our recent analysis of the more complicated Zr($4d^25s^2$, ^3F) + ethylene reaction.[10] In that system, both triplet and singlet spin surfaces are probably important. RRKM calculations based on the *m*PW1PW91 energies ($^3\mathbf{TS_{ins}}$ and $^1\mathbf{TS_{ins}}$ at −6.2 and −15.3 kcal/mol, respectively) indicate that facile CH bond insertion on either the triplet or singlet surface is in accord with the measured isotope effect $k_H/k_D = 1.04 \pm 0.05$ and the absence of stabilized ZrC_2H_4 or ZrC_2D_4 complexes at low collision energies. The competition between dissociation and insertion on the triplet surface with the unknown triplet-to-singlet intersystem crossing rate k_{ISC} then determines the branching between the two surfaces, as discussed earlier.[10] In contrast to Y + ethylene, essentially all Zr(ethylene) collision complexes react since k_{ins} dominates, i.e., B ∼ 1. If the *m*PW1PW91 functional is correct in finding no barrier to the approach of ground-state Zr with ethylene, then the measured 7% reaction inefficiency must be attributed entirely to nonadiabatic/steric effects. Consequently, the factor *A* becomes 0.07, similar to the factor necessary to explain the reduced efficiency of Y + ethylene.

VI. Conclusion

The identification of reaction products and determination of kinetic isotope effects for Y ($4d^15s^2$, ^2D) with ethylene and propylene provides much needed experimental data from which to infer reaction mechanisms. New density functional theory calculations sharpen the theoretical view of the Y + ethylene system, including explicit characterization of all reaction intermediates and transition states along the doublet PES. A new lowest-energy path involving the concerted elimination of H_2 was identified, consistent with the observation of YC_2H_2 products.

In the absence of an approach barrier, as suggested by theory, a statistical rate model is able to explain all of the experimental data with essentially no adjustments of the *m*PW1PW91 energetics calculated for primary CH bond insertion. A second model that includes the effects of a rate-determining approach barrier demands somewhat larger adjustments (+2 to +5 kcal/mol). Once again, both models indicate that B3LYP overestimates $^2\mathbf{TS_{ins}}$ by at least 6−9 kcal/mol, comparable to its performance on other related systems.[24−27,10] Therefore, this study provides additional evidence that *m*PW1PW91 more accurately describes the energetics of electronically complex transition metal−hydrocarbon species. The results are satisfyingly consistent with recent experimental and theoretical studies of Zr ($4d^25s^2$, ^3F) + ethylene.[10]

Despite the more detailed understanding of transition metal−alkene chemistry afforded by such work, the issue of room-temperature reaction inefficiency remains unresolved. Nonadiabatic and steric effects may both contribute, and we cannot rule out the possibility that some or all of the reaction inefficiency is due to a small approach barrier along the adiabatic entrance channel for both Y($4d^15s^2$, ^2D) and Zr($4d^25s^2$, ^3F) reactions with ethylene. If so, density functional theory fails to capture the long-range energetics. More sophisticated multiconfigurational methods may be required to accurately describe the subtle transition metal−hydrocarbon long-range potential. The definitive answer will come from *experimental* studies of the Y + ethylene and Zr + ethylene reactions using a variable-temperature flow reactor or a merged-beam apparatus at very low collision energies (<1 kcal/mol).

Finally, additional studies in progress[52,53] will help provide a unified picture of the interactions of neutral transition metals with small alkenes. Y + propylene has four unique bond insertion possibilities; perhaps CC bond activation is important or some of the CH insertion barriers are significantly lower than in Y + ethylene. In contrast to Y and Zr, ground-state Nb ($4d^4$-$5s^1$, ^6D) has an s^1 configuration which is expected to be more strongly attractive to alkenes. In Nb, the interplay of the low-lying sextet and quartet spin surfaces will likely be important in determining the reaction efficiency, analogous to the two surfaces in play for Zr.

Acknowledgment. Generous support of this research has come from the National Science Foundation (Grants CHE-9616724 and NSF-0071458) and the donors of the Petroleum Research Fund (Grant 33441-AC6). M.P. thanks the UW-Madison Department of Chemistry for a Martha Weeks graduate fellowship.

Supporting Information Available: Rotational constants and vibrational frequencies of all stationary points calculated at the B3LYP/Stuttgart+6-311++G(d,p) level. This material is available free of charge via the Internet at http://pubs.acs.org.

References and Notes

(1) Mitchell, S. A. In *Gas-Phase Metal Reactions*; Fontijn, A., Ed.; Elsevier: Amsterdam, 1992.

(2) Carroll, J. J.; Haug, K. L.; Weisshaar, J. C. *J. Am. Chem. Soc.* **1993**, *115*, 6962.

(3) Carroll, J. J.; Haug, K. L.; Weisshaar, J. C.; Blomberg, M. R. A.; Siegbahn, P. E. M.; Svensson, M. *J. Phys. Chem.* **1995**, *99*, 13955.

(4) Parnis, J. M.; Lafleur, R. D.; Rayner, D. M. *J. Phys. Chem.* **1995**, *99*, 673.

(5) Wen, Y.; Porembski, M.; Ferrett, T. A.; Weisshaar, J. C. *J. Phys. Chem. A* **1998**, *102*, 8362.

(6) Porembski, M.; Weisshaar, J. C. *J. Phys. Chem. A* **2000**, *104*, 1524.

(7) Willis, P. A.; Stauffer, H. U.; Hinrichs, R. Z.; Davis, H. F. *J. Phys. Chem. A* **1999**, *103*, 3706.

(8) Stauffer, H. U.; Hinrichs, R. Z.; Willis, P. A.; Davis, H. F. *J. Chem. Phys.* **1999**, *111*, 4101.

(9) Stauffer, H. U.; Hinrichs, R. Z.; Schroden, J. J.; Davis, H. F. *J. Phys. Chem. A* **2000**, *104*, 1107.

(10) Porembski, M.; Weisshaar, J. C. *J. Phys. Chem. A* **2001**, *105*, 4851.

(11) Blomberg, M. R. A.; Siegbahn, P. E. M.; Svensson, M. *J. Phys. Chem.* **1992**, *96*, 9794.

(12) Siegbahn, P. E. M.; Blomberg, M. R. A.; Svensson, M. *J. Am. Chem. Soc.* **1993**, *115*, 1952.

(13) Siegbahn, P. E. M. *J. Am. Chem. Soc.* **1993**, *115*, 5803.

(14) Siegbahn, P. E. M. *Chem. Phys. Lett.* **1993**, *205*, 290.

(15) Siegbahn, P. E. M. *Theor. Chim. Acta* **1994**, *87*, 277.

(16) Siegbahn, P. E. M. *J. Organomet. Chem.* **1994**.

(17) Niu, S.; Hall, M. B. *Chem. Rev.* **2000**, *100*, 353.

(18) Ziegler, K.; Holzkamp, E.; Breil, H.; Martin, H. *Angew. Chem.* **1955**, *67*, 541.

(19) Natta, G. *Macromol. Chem.* **1955**, *16*, 213.

(20) Pasquon, I.; Giannini, U. In *Catalysis: Science and Technology*; Anderson, J. R., Boudart, M., Eds.; Springer-Verlag: Heidelberg, 1984; Vol. 6, p 65.

(21) Becke, A. D. *J. Chem. Phys.* **1993**, *98*, 1372.

(22) Adamo, C.; Barone, V. *Chem. Phys. Lett.* **1997**, *274*, 242.

(23) Adamo, C.; Barone, V. *J. Chem. Phys.* **1998**, *108*, 664.

(24) Yi, S. S.; Blomberg, M. R. A.; Siegbahn, P. E. M.; Weisshaar, J. C. *J. Phys. Chem. A* **1998**, *102*, 395.

(25) Blomberg, M. R. A.; Siegbahn, P. E. M.; Yi, S. S.; Noll, R. J.; Weisshaar, J. C. *J. Phys. Chem. A* **1999**, *103*, 7254.

(26) Reichert, E. L.; Yi, S. S.; Weisshaar, J. C. *Int. J. Mass Spectrom.* **2000**, *196*, 55.

(27) Yi, S. S.; Reichert, E. L.; Holthausen, M. C.; Koch, W.; Weisshaar, J. C. *Chem.-Eur. J.* **2000**, *6*, 2232.

(28) Gilbert, R. G.; Smith, S. C. *Theory of Unimolecular and Recombination Reactions*; Blackwell Scientific Publications: Oxford, U.K., 1990.

(29) Baer, T.; Hase, W. L. *Unimolecular reaction dynamics*; Oxford University Press: New York, 1996.

(30) Tolbert, M. A.; Beauchamp, J. L. *J. Am. Chem. Soc.* **1986**, *108*, 7509.

(31) Tonkyn, R.; Ronan, M.; Weisshaar, J. C. *J. Phys. Chem.* **1988**, *92*, 92.

(32) Lech, L. M.; Freiser, B. S. *Organometallics* **1988**, *7*, 1948.

(33) Sunderlin, L.; Aristov, N.; Armentrout, P. B. *J. Am. Chem. Soc.* **1987**, *109*, 78.

(34) Sunderlin, L.; Armentrout, P. *Int. J. Mass Spectrom. Ion Processes* **1989**, *94*, 149.

(35) Sunderlin, L.; Armentrout, P. *Organometallics* **1990**, *9*, 1248.

(36) Sanders, L.; Hanton, S. D.; Weisshaar, J. C. *J. Chem. Phys.* **1990**, *92*, 3498.

(37) Fisher, E. R.; Armentrout, P. B. *J. Am. Chem. Soc.* **1992**, *114*, 2039.

(38) van Koppen, P.; Bowers, M.; Haynes, C.; Armentrout, P. *J. Am. Chem. Soc.* **1998**, *120*, 5704.

(39) Andrae, D.; Haussermann, U.; Dolg, M.; Stoll, H.; Preuss, H. *Theor. Chim. Acta* **1990**, *77*, 123.

(40) Frisch, M. J.; Trucks, G. W.; Schlegel, H. B.; Scuseria, G. E.; Robb, M. A.; Cheeseman, J. R.; Zakrzewski, V. G.; Montgomery, J. A.; Stratmann, R. E.; Burant, J. C.; Dapprich, S.; Millam, J. M.; Daniels, A. D.; Kudin, K. N.; Strain, M. C.; Farkas, O.; Tomasi, J.; Barone, V.; Cossi, M.; Cammi, R.; Mennucci, B.; Pomelli, C.; Adamo, C.; Clifford, S.; Ochterski, J.; Petersson, G. A.; Ayala, P. Y.; Cui, Q.; Morokuma, K.; Malick, D. K.; Rabuck, A. D.; Raghavachari, K.; Foresman, J. B.; Cioslowski, J.; Ortiz, J. V.; Stefanov, B. B.; Liu, G.; Liashenko, A.; Piskorz, P.; Komaromi, I.; Gomperts, R.; Martin, R. L.; Fox, D. J.; Keith, T.; Al-Laham, M. A.; Peng, C. Y.; Nanayakkara, A.; Gonzalez, C.; Challacombe, M.; Gill, P. M. W.; Johnson, B.; Chen, W.; Wong, M. W.; Andres, J. L.; Head-Gordon, M.; Replogle, E. S.; Pople, J. A. Gaussian 98, Revision A.6:; Gaussian, Inc.: Pittsburgh, PA, 1998.

(41) Hay, P. J.; Wadt, W. R. *J. Chem. Phys.* **1985**, *82*, 270.

(42) Koch, W.; Holthausen, M. C. *A chemist's guide to density functional theory*; Wiley-VCH: New York, 2000.

(43) Moore, C. E. *NBS Circ. No. 467*; U. S. Department of Commerce: Washington, D. C., 1949; Vol. I−III.

(44) Koch, W.; Hertwig, R. H. Density functional theory applications to transition metal problems. In *Encyclopedia of Computational Chemistry*; Schleyer, P., Ed.; John Wiley: New York, 1998; Vol. 1, p 689.

(45) Glendening, E. D.; Badenhoop, J. K.; Reed, A. E.; Carpenter, J. E.; Weinhold, F. NBO 5.0; 5.0 ed.; Theoretical Chemistry Institute: University of Wisconsin−Madison, 1998.

(46) Schwenke, D. W.; Truhlar, D. G. *J. Chem. Phys.* **1985**, *82*, 2418.

(47) Carroll, J. J. Kinetics and Mechanisms of Gas-Phase Reactions of Transition Metal Atoms with Small Hydrocarbons, University of Wisconsin−Madison, 1995.

(48) Holthausen, M. C.; Fiedler, A.; Schwarz, H.; Koch, W. *J. Phys. Chem.* **1996**, *100*, 6236.

(49) Holthausen, M. C.; Koch, W. *J. Am. Chem. Soc.* **1996**, *118*, 9932.

(50) Holthausen, M. C.; Koch, W. *Helv. Chim. Acta* **1996**, *79*, 1939.

(51) Carroll, J. J.; Weisshaar, J. C.; Siegbahn, P. E. M.; Wittborn, C. A. M.; Blomberg, M. R. A. *J. Phys. Chem.* **1995**, *99*, 14388.

(52) Porembski, M.; Weisshaar, J. C. *J. Phys. Chem. A*, to be submitted (work in progress).

(53) Porembski, M.; Weisshaar, J. C. *J. Phys. Chem. A*, to be submitted (work in progress).